

# Riblet surface effect on laminar to turbulent transition by Direct Numerical Simulation

Kento Kaneko<sup>1</sup>, Akira Oyama<sup>2</sup>, Aiko Yakeno<sup>3</sup> and Shingo Hamada<sup>3</sup>

<sup>1</sup> The University of Tokyo, Sagamihara, Kanagawa, 252-5210, Japan

<sup>2</sup> Institute of Space and Astronautical Science, JAXA, Sagamihara, Kanagawa, 252-5210, Japan

<sup>3</sup> Tohoku University, Sendai, Miyagi, 980-8577, Japan

<sup>1</sup> Corresponding Author [kkaneko@flab.isas.jaxa.jp](mailto:kkaneko@flab.isas.jaxa.jp)

## Abstract

Direct numerical simulations of the laminar, transition, and turbulent flows at the speed of the aircraft cruise condition are carried out to reveal the effect of the riblet on the drag. The drag decreases in the transition and turbulent regions while it increases in the laminar region on the riblet surface compared to the smooth surface. The main reason for the change in the drag is that the riblet changes the friction drag coefficient. Since the shear stresses in turbulent flow are broadly divided into kinematic viscosity and stresses due to turbulence fluctuation, the effect of the riblet on each of these stresses is investigated. The mean velocity profiles show that the stress due to kinematic viscosity is reduced on the riblet surface compared to the smooth surface in the laminar, transition, and turbulent flow regions. In the laminar flow regime, only the reduction of the kinematic viscous stresses is apparent as an effect of the riblet. This effect is not sufficient to reduce drag enough to overcome the increase in wetted area. On the other hand, in the transition and the turbulent regions, not only the kinematic viscous stresses but also the stresses due to turbulent fluctuations are reduced by the riblet, resulting in the reduction of the drag. Under the presented computational conditions, the rate of drag reduction is greater in the transition region than in the turbulent region. One of the reasons for this is that the reduction in friction drag due to the turbulence fluctuation is greater in the transition region than in the turbulent region. The investigation of the turbulence statistics suggests that the riblet promotes three-dimensional collapse before the T-S waves grow strongly. Therefore, the turbulent kinetic energy is suppressed by the riblet in the transition region. It is conceivable that there is a correlation between the reduction in the turbulent kinetic energy and the reduction in the friction drag due to the turbulent fluctuation.

## Nomenclature

$A_f$	=	fluid-occupied area at a certain height over the riblet surface
$C_d$	=	drag coefficient at a certain time $t$
$C_D$	=	time-averaged drag coefficient
$C_f$	=	local skin friction coefficient at a certain time $t$
$C_F$	=	time-averaged local skin friction coefficient
$CR_D$	=	change rate of drag between those over the smooth and the riblet surfaces
$C_T$	=	weighted integral of Reynolds shear stress
$d$	=	drag at a certain time $t$
$\delta_{in}$	=	laminar boundary layer thickness at the inlet boundary
$\mathbf{e}_z$	=	unit vector in the wall-normal direction
$F$	=	frequency of disturbance
$h$	=	riblet maximum height
$h^+$	=	dimensional riblet height
$ll$	=	factor for same wetted area on smooth and riblet surface
$L_x$	=	length of computational domain in the streamwise direction
$L_y$	=	length of computational domain in the spanwise direction
$L_z$	=	length of computational domain in the wall-normal direction
$\mathbf{n}_w$	=	wall-normal vector at a certain time $t$
$N_x$	=	number of grid points in the streamwise direction
$N_y$	=	number of grid points in the spanwise direction
$N_z$	=	number of grid points domain in the wall-normal direction

$\nu$	=	kinematic viscosity
$\emptyset$	=	ratio of the fluid-occupied area
$Re_{\delta_{in}}$	=	Reynolds number based on $\delta_{in}$
$Re_x$	=	Reynolds number based on $x$
$\rho$	=	density
$s$	=	riblet width
$s^+$	=	dimensional riblet width
$S$	=	reference surface area
$t$	=	non-dimensional time
$T$	=	non-dimensional time used for time average
$T_s$	=	non-dimensional start time used for time average
$\boldsymbol{\tau}_w$	=	local stress tensor at a certain time $t$
$u$	=	velocity in the streamwise direction
$u_{rms}$	=	root-mean-square velocity fluctuations in the streamwise direction
$u_\tau$	=	friction velocity
$v$	=	velocity in the spanwise direction
$v_{rms}$	=	root-mean-square velocity fluctuations in the spanwise direction
$w$	=	velocity in the wall-normal direction
$w'$	=	disturbance in the wall-normal direction
$w_b$	=	velocity in the wall-normal direction obtained by the incompressible Blasius laminar flow solution
$w_{rms}$	=	root-mean-square velocity fluctuations in the wall-normal direction
$x$	=	coordinate in the streamwise direction
$y$	=	coordinate in the spanwise direction
$z$	=	coordinate in the wall-normal direction

### Subscript

$in$	=	value at the inlet
$riblet$	=	value on the riblet surface
$smooth$	=	Value in the smooth surface
$\infty$	=	freestream value

## 1. Introduction

In recent years, the growing issue of increased CO<sub>2</sub> emissions from aircraft has raised significant concerns. One of the solutions to this problem is to reduce the aerodynamic drag of aircraft. Even a drag reduction as small as 1% from a civilian aircraft can translate to significant long-term savings in CO<sub>2</sub> emissions [1]. In the aerodynamic drag of a transonic aircraft, the frictional drag accounts for a large amount of the drag, approximately 50 % [2]. Reducing friction drag is therefore an effective means of reducing CO<sub>2</sub> emissions from aircraft.

Laminarization and turbulence control techniques are representative examples of methods to reduce friction drag. Laminarization is generally achieved by keeping the flow in a laminar or quasi-stable state and delaying the turbulent transition. On the other hand, turbulence control is the technique of reducing drag by changing the turbulence structure in the turbulent region.

In some cases, laminarisation is achieved by a large-scale modification of the shape. For example, the HondaJet, a business jet developed by Honda in recent years, incorporates laminarization technology [3]. The shape of the HondaJet's wing and the fuselage nose were designed through extensive analyses and wind-tunnel tests. This technology should be considered for new aircraft designs as the drag reduction is achieved without the special equipment required. However, it is difficult to make major modifications to the wing and the nose shape of existing passenger aircraft. In contrast, a microroughness structure has been attracting attention as one of the potential ways to delay the transition and reduce viscous drag without major shape modification [4,5]. Hamada et al. [6] examined the effects of a wavy rough surface and a sand-grind rough surface on the laminar-turbulent transition over Tollmien-Schlichting (T-S) waves by Direct Numerical Simulations, hereafter denote as DNSs. They found that the T-S waves are weaker on the wavy rough surface and the random sand-grind surface than on the smooth surface. It was also found that the total turbulent kinetic energy is reduced on the sand-grind rough surface compared to other surfaces, while the breaking up of the T-S wave is enhanced. These results suggest that microroughness structures could reduce the frictional drag reduction. Determining the optimal shape to achieve the most effective reduction in viscous drag through microroughness structures remains an area of ongoing fundamental research.

The most notable example of turbulence control is a riblet. Riblets are fine longitudinal grooves fabricated in the streamwise direction, i.e., no major geometry changes are required. Over many years, the drag-reducing effect of riblets have been investigated, for example, by the NASA Langley Research Center [7,8], the German Aerospace Center Berlin DLR [9,10], and JAXA [11,12]. Furthermore, with the recent improvements in the manufacturing technology, riblets are getting more and more attention [13]. It has been reported that riblets have a maximum drag reduction effect of approximately 10% in the turbulent region of the boundary layer [14-16]. Walsh et al. [17] conducted extensive experiments and found that the drag reduction effect of riblets is observed at  $s^+ = su_\tau/\nu = 3\sim 30$  and  $h^+ = hu_\tau/\nu = 4\sim 15$ , where  $s$  and  $h$  are the width and height of riblets, and  $\nu$  and  $u_\tau$  denote the kinematic viscosity and the wall-shear velocity, respectively. Choi et al. [18] and Lee et al. [19] observed flow fields around riblets in turbulent boundary layers. They found that longitudinal vortices on the riblet surface were kept away relative to the smooth surface, leading to drag reduction in the turbulent region. Suzuki et al. [20] measured the statistics of all three velocity components on a riblet surface in a turbulent boundary layer and compared them with those above a smooth surface. They found that all of the turbulent velocity fluctuations and the Reynolds shear stress were decreased near the riblet surface under a drag-reducing condition. Their findings support the observations by Choi et al [18]. Most of the studies have been in low-speed ground facilities; however, some flight tests have also been carried out in which a riblet has been applied to parts of the aircraft's fuselage [12, 21]. Although there are only a few examples, it has been shown that the riblet has a drag-reducing effect even under flight conditions.

Both laminarization and turbulence control are expected to be realized by surface properties and have been studied independently. However, riblets have also been studied in the laminar flow and transition regions. Djenidi et al. [22,23], Choi et al. [24], Raayai et al. [25], and Kaneko et al. [26] have investigated the effect of the riblet on the drag in the laminar flow, and all agree that the drag is basically increased, except for certain cases. Raayai et al. [25] and Kaneko et al. [26] found that, independent of interference with turbulent structures, the riblets have the function of creating almost stagnant regions in the trough and thereby making the velocity-gradient near the wall milder. Regarding the transition region, Ladd et al. [27] investigated the effect of a riblet of  $s^+ < 6$  on the transition location in an incompressible flow using a laser Doppler velocimeter. The results showed that a riblet of  $s^+ < 6$  slightly accelerates the transition. On the other hand, Grek et al. [28] investigated experimentally for a riblet of  $s^+ \approx 20$  and found that the riblet slightly delayed the transition. On the contrast, Klumpp et al. [29] conducted LES analysis for riblets of  $s^+ \approx 20$ . Their conclusion is in agreement with Grek et al. [28] in that the riblet does not dramatically affect the transition location. In summary, the influence of the riblet on the transition location has been discussed. However, the effect of the riblet on the viscous drag in the transition flow has not been investigated.

Laminar, transition, and turbulent flows exist in the fuselage nose and wings of aircraft. In order to apply the riblet to aircraft efficiently, it is important to investigate the effect of the riblet on drag in such flows. Therefore, in this study, DNSs are conducted with the aim of clarifying the drag reduction performance of the riblet in the laminar, transition, and turbulent flow.

## 2. Computational Setup

### 2.1 Geometry

In this study, numerical computations are carried out on both smooth and riblet surfaces, and their results are compared. Figure 1 shows a schematic of the computational domain, and Table 1 summarizes the size of the computational domain. As shown in Figure 1,  $x$  is streamwise direction,  $y$  is spanwise direction, and  $z$  is wall-normal direction, respectively. As for the geometry of the riblet, an equilateral triangle is adopted for the cross-sectional shape of the riblet. The cross-sectional shape is constant in the streamwise direction. Regarding the dimension of the groove width of the riblet, the dimensionless groove width  $s^+$  is set to be approximately 13 in the turbulent regions. It is known that the drag decreases in turbulent flow regions on the riblet surface with  $s^+ \approx 13$  [17]. The groove width relative to the boundary layer thickness at the inlet is approximately  $0.085\delta_{in}$ .

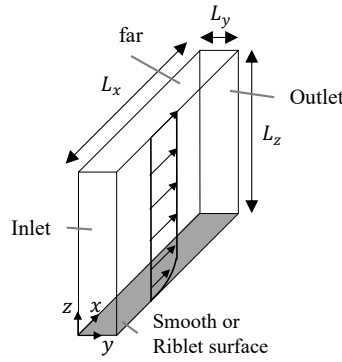


Figure 1 : Schematic of the geometry

Table 1 : Computational domain

	$L_x$	$L_y$	$L_z$
Smooth surface	$56.6\delta_{in}$	$8.49\delta_{in}$	$28.3\delta_{in}$
Riblet surface	$56.6\delta_{in}$	$2.04\delta_{in}$ (= 24 ribs)	$28.3\delta_{in}$

## 2.2 Flow Conditions

The Reynolds number  $Re_{\delta_{in}}$  based on the boundary layer thickness  $\delta_{in}$  at the inlet boundary is set to 3500 to include laminar, transition, and turbulent flow regions in the computational domain.  $Re_{\delta_{in}} = 3500$  corresponds to  $Re_x \approx 4.9 \times 10^5 \sim 6.9 \times 10^5$  by considering the Reynolds number  $Re_x$  based on the length in the streamwise direction as shown in Figure 2. In Figure 2,  $x = 140\delta_{in} \sim 196.6\delta_{in}$  is the computational domain in this analysis, while  $x = 0 \sim 140\delta_{in}$  represents the region between the leading edge of the surface and inlet boundary of the computational domain. The Mach number  $M_\infty$  is set to  $M_\infty = 0.85$ .  $M_\infty = 0.85$  represents a transonic flight of passenger aircraft.

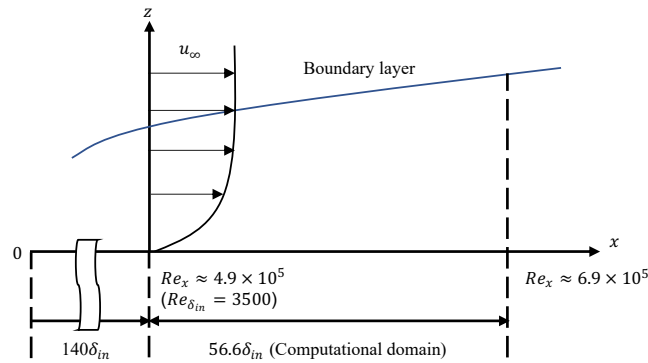


Figure 2 : The schematic of the computational domain and flow conditions

## 2.3 Boundary Conditions

On the smooth and riblet surfaces, the non-slip wall condition is applied, i.e., the velocity is fixed to zero in all directions. On the wall surface, the adiabatic wall condition is assumed, and furthermore, the density and pressure are set to zero gradient in the wall-normal direction. The velocity profile of the incompressible Blasius laminar layer is used at the streamwise inlet boundary. Additionally, an artificial disturbance  $w'(z)$  is added to the inlet boundary to induce T-S waves. The artificial disturbance  $w'(z)$  is defined by equation (1). Hence the wall-normal velocity at the inlet  $w_{in}(z)$  is defined by equation (2).

$$w'(z) = 800 \left( w_b(\infty) - w_b(z) \right) \sin 2\pi \left( Ft + \frac{z}{\delta_{in}} \right) \quad (1)$$

$$w_{in}(z) = w_b(z) + w'(z) \quad (2)$$

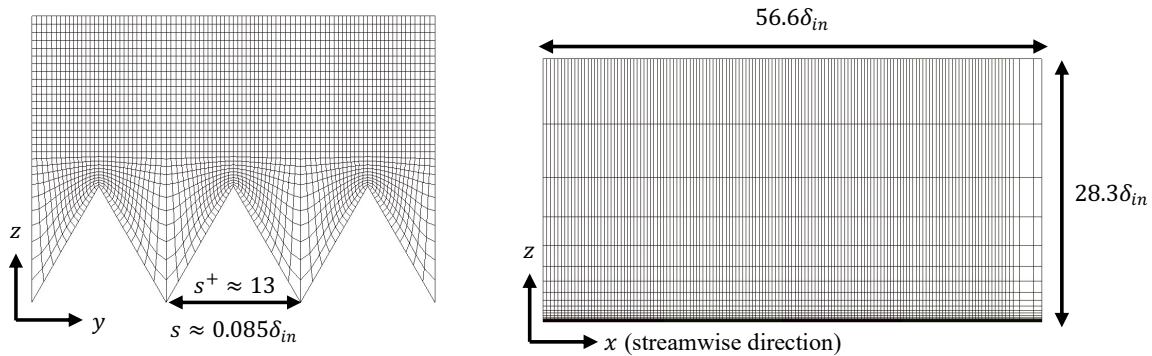
In equation (1), the frequency  $F$  is set to 0.025. It is included in the unstable frequency for the Reynolds number  $Re_{\delta_{in}} = 3500$ . To make the maximum amplitude of the wall normal velocity  $w_{in}$  the same order as the free-stream velocity  $u_{\infty}$ ,  $(w_b(\infty) - w_b(z))$  is multiplied by 800. At the outlet boundary, Dirichlet conditions are applied for density, pressure, and velocity in the streamwise direction. The 2nd order low-pass filter is also applied to the outlet boundary. At the far boundary, the pressure and streamwise velocity are fixed to the free-stream values, while the velocity in the wall-normal and spanwise directions are Dirichlet conditions. A periodic boundary condition is applied to the spanwise boundary.

## 2.4 Computational methods

The governing equations are the three-dimensional compressible Navier-Stokes equations. In this study, Direct Numerical Simulations (DNSs) are conducted by using LANS3D [30]. The spatial derivatives of the convective and viscous terms are evaluated by the 6th order compact different scheme [31] with the 10th order low-pass filtering [32]. The filter coefficient is set to be 0.495. The metrics, and Jacobians are also computed by the 6th order compact different scheme. As for the time integration, the three-step TVD Runge-Kutta method [33] is adopted.

## 2.5 Computational grid

The cross-sectional view of the grid around the riblet and the side view of the grid at the valley of the riblet is shown in Figure 3. The riblet has 16 grid points per side of the rib in the spanwise direction as shown in Figure 3(a). In Figure 3(b), every 10 points are displayed in both  $x$ - and  $z$ -directions. The number of grid points for the smooth surface and riblet surface analyses is given in Table 2. The grid spacing is  $\Delta x^+ < 15$ ,  $\Delta y^+ < 4$ ,  $\Delta z^+ < 0.5$  in most regions. In comparison to recent DNSs of open channel flow [34], the computational grid used in this study is fine enough to resolve longitudinal vortices.



(a) The cross-sectional view of the grid around the riblet (b) the side view of the grid at the valley of the riblet. Every 10 points are displayed in both  $x$ - and  $z$ -directions.

Figure 3 : Computational grid of the riblets

Table 2 : Number of grid points

	$N_x$	$N_y$	$N_z$	Total
Smooth surface	1,453	201	204	59,578,812
Riblet surface	1,453	721	204	213,713,052

## 2.6 Evaluation methods

The effect of drag changes due to riblets is the objective of this study. Therefore, the main discussion is focused on the time-averaged coefficient of skin friction  $C_F$ , the coefficient of drag  $C_D$  and the rate of change  $CR_D$  of the drag between the smooth surface and riblet surface in the final one flow-through. Note that, the time step that the flow reaches from the inlet to the outlet is taken as one flow-through, and more than 6 flow-throughs are calculated to ensure adequate convergence of the solution in this study.

The local skin friction coefficient  $C_F$  is calculated from equations (3) and (4) with the local stress tensor  $\boldsymbol{\tau}_w(x, y, t; z)$  and the local wall-normal vector  $\mathbf{n}_w(x, y, t; z)$  at a certain time and location  $(x, y, t; z)$ .

$$C_f(x, y, t; z) = \boldsymbol{\tau}_w(x, y, t; z) \cdot \mathbf{n}_w(x, y, t; z) \cdot \mathbf{e}_z \quad (3)$$

$$C_F(x, y; z) = \frac{1}{T} \int_{T_s}^{T_s+T} C_f(x, y, t; z) dt \quad (4)$$

The drag coefficient  $C_D$  is calculated from equations (5) and (6) with  $C_f(x, y, t; z)$  at a certain time and location  $(x, y, t; z)$ . In equation (5),  $d(t)$  is the drag at a certain time obtained from surface integration of  $C_f(x, y, t; z)$ .

$$d(t) = \int_S C_f(x, y, t; z) dS \quad (5)$$

$$C_D = \frac{\frac{1}{T} \int_{T_s}^{T_s+T} D(t) dt}{\frac{1}{2} \rho_\infty u_\infty^2 S} \quad (6)$$

Equations (7) and (8) are used to calculate the change ratio of drag  $CR_D$  between the smooth and the riblet surface.

$$\begin{aligned} \Delta C_D &= \frac{1}{T} \int_{T_s}^{T_s+T} (C_{d_{riblet}}(t) - C_{d_{smooth}}(t)) dt \\ &= \frac{2}{\rho_\infty u_\infty^2 T} \int_{T_s}^{T_s+T} \left( \frac{\int_{S_{riblet}} C_{f_{riblet}}(z, y, t; z) dS_{riblet}}{S_{riblet}} \times ll - \frac{\int_{S_{smooth}} C_{f_{smooth}}(z, y, t; z) dS_{smooth}}{S_{smooth}} \right) dt \end{aligned} \quad (7)$$

$$CR_D = \frac{\Delta C_D}{C_{D_{smooth}}} \times 100 \quad (8)$$

In equation (7),  $ll$  is a coefficient that takes into account the increased wetting area on the riblet surface,  $ll = (s^2 + 4h^2)^{1/2}/s$ .

## 2.7 Spanwise averaging methods

In this study, the analysis is performed using a boundary-fitted grid as shown in Figure 3. Therefore, the flow field data is mapped once on the orthogonal grid and then an averaging process is undertaken in the spanwise direction. Furthermore, in the case that the wall surface geometry changes in the span direction, such as a riblet surface. It should be noted that both the fluid and solid wall regions exist in the spanwise direction. The spanwise averaging process is defined by Equation (9) [35]. Here,  $\phi(z) = A_f/L_y$  is ratio of the fluid-occupied area,  $A_f$ , to the total area. In the case of the  $z$ -direction higher than the rib tip,  $\phi = 1$ , while below the rib tip,  $\phi < 1$ . In the case of  $\phi = 0$  at the rib valley, the velocity is set to zero to avoid divergence of the physical quantities.

$$\overline{q(z)} = \frac{1}{\phi(z)} \frac{1}{L_y} \int_0^{L_y} q(z) dy \quad (9)$$

## 3. Results and discussion

### 3.1 Instantaneous flow field

From the visualisation in the instantaneous flow field, the state of the flow field is first examined. In Figure 4, the instantaneous iso-surfaces of the second invariant of the velocity gradient tensor around both of the smooth surface and the riblet surface are visualized from the top view at  $x/\delta_{in} = 140 \sim 166.1$ . The flow is in the right direction on the paper.

The visualizations indicate that the laminar, transition, and turbulent flow structure via the T-S waves are simulated by the present DNSs on both smooth surface and the riblet surface. The location of the beginning of the TS wave collapse does not seem to change dramatically between the smooth and riblet surfaces.

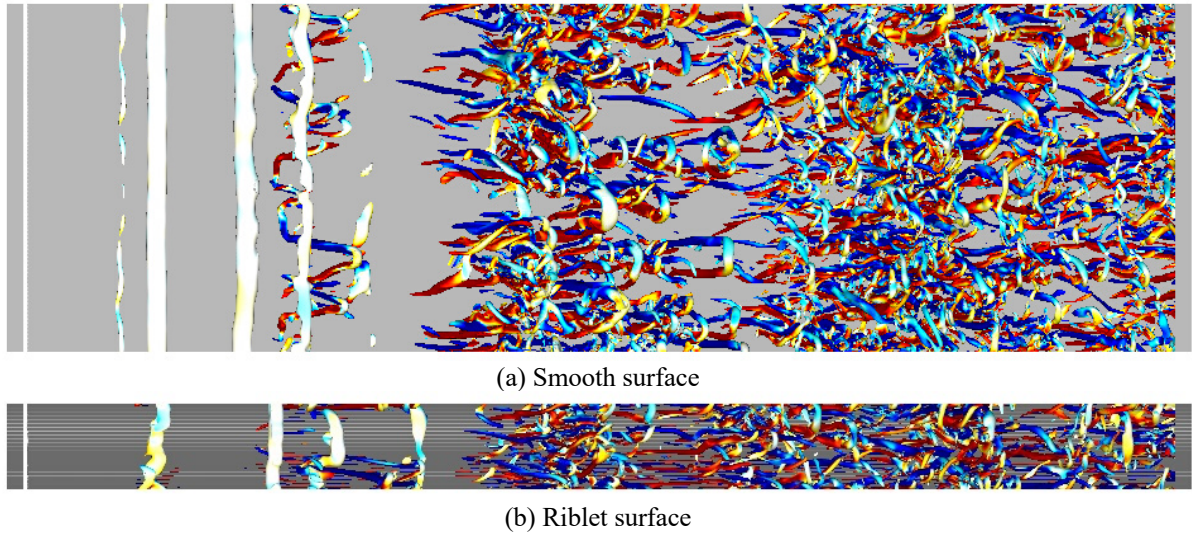


Figure 4 : Instantaneous iso-surfaces of the second invariant of velocity gradient tensor;  $Q = 0.05$  colored by the streamwise vorticity from the top view

### 3.2 Turbulence intensities and Turbulent Kinetic Energy

In this section, the entire flow field is observed from the basic turbulence statistics.

To begin with, the visualisations of the  $u_{rms}$  are shown in Figure 5. Figure 5 shows a side view of the region  $x/\delta_{in} = 140 \sim 196.6$ , with the flow direction to the right of the paper. The vertical distribution of  $u_{rms}$  at  $x/\delta_{in} = 145.2$ , 155.6 and 189.4 are also shown in Figure 6.

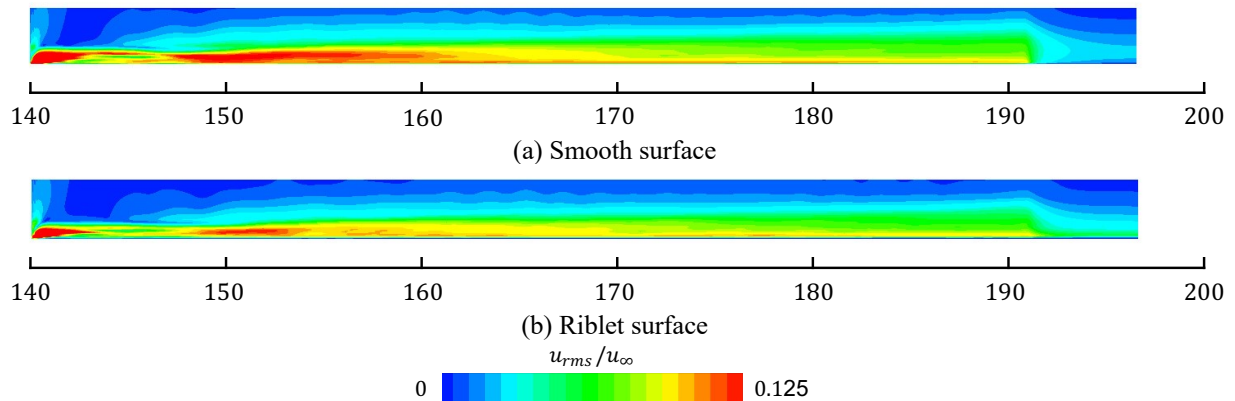


Figure 5 : Side view contour maps of the time- and spanwise-averaged  $u_{rms}$

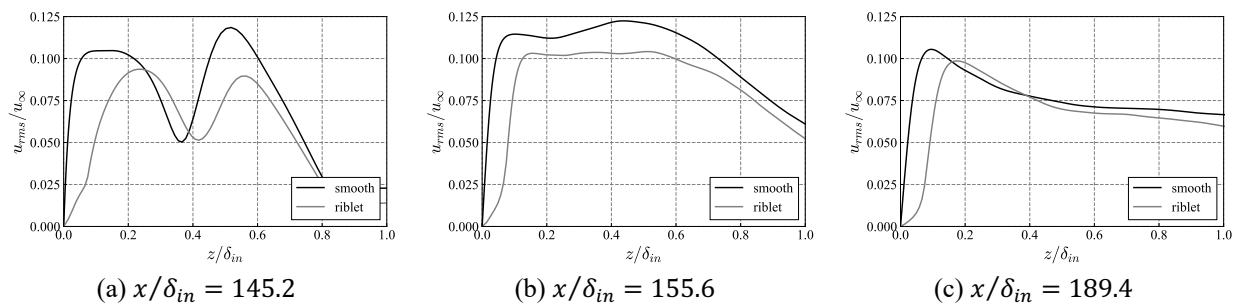


Figure 6 : The time- and spanwise-averaged  $u_{rms}$  profile

Figure 5 indicates that in the region  $x/\delta_{in} \approx 140\sim 165$ , the  $u_{rms}$  values tend to be decrease on the riblet surface compared to on the smooth surface. In addition, as shown in Figure 6(a), there are two peaks at  $x/\delta_{in} = 145.2$ , suggesting the existence of spanwise vortices on both surfaces; the two peak values are both smaller on the riblet surface than on the smooth surface, and their distance from the wall surface is farther. On the other hand, for  $x/\delta_{in} = 189.4$ , the shape of the distribution is typical of turbulent regions [18, 20]. In turbulent regions, the peak values are larger on smooth surfaces. The peak distance from the wall is farther away on the riblet surface than on the smooth surface.  $x/\delta_{in} = 155.6$  is considered to be the transition region, with lower values on the riblet surface than on the smooth surface at any height position.

Secondly, the visualisations of the  $v_{rms}$  are shown in Figure 7. Figure 7 shows a side view of the region  $x/\delta_{in} = 140\sim 196.6$ , with the flow direction to the right of the paper. The vertical distribution of  $v_{rms}$  at  $x/\delta_{in} = 145.2, 155.6$  and  $189.4$  are also shown in Figure 8.

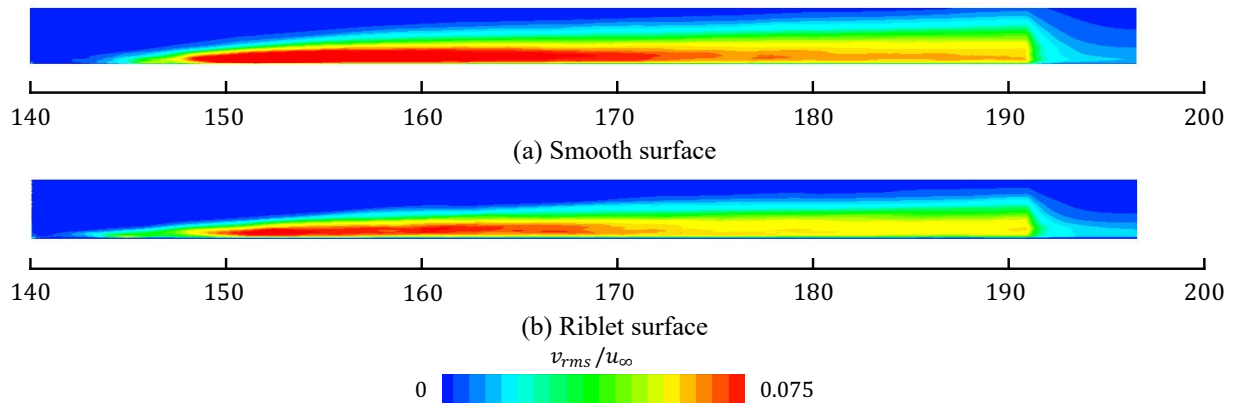


Figure 7 : Side view contour maps of the time- and spanwise-averaged  $v_{rms}$

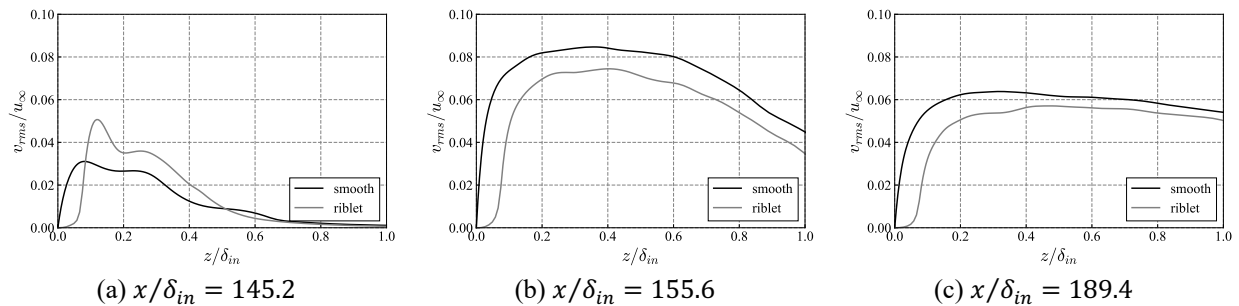
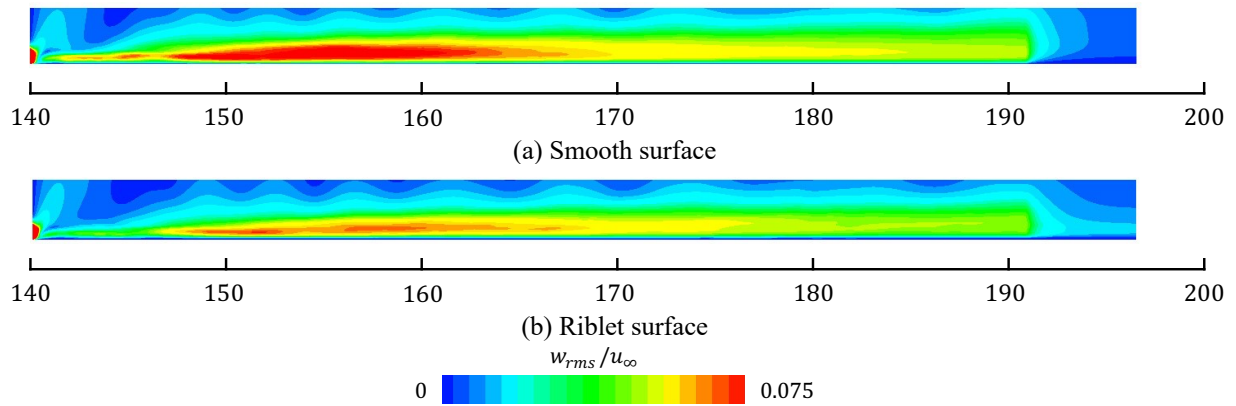
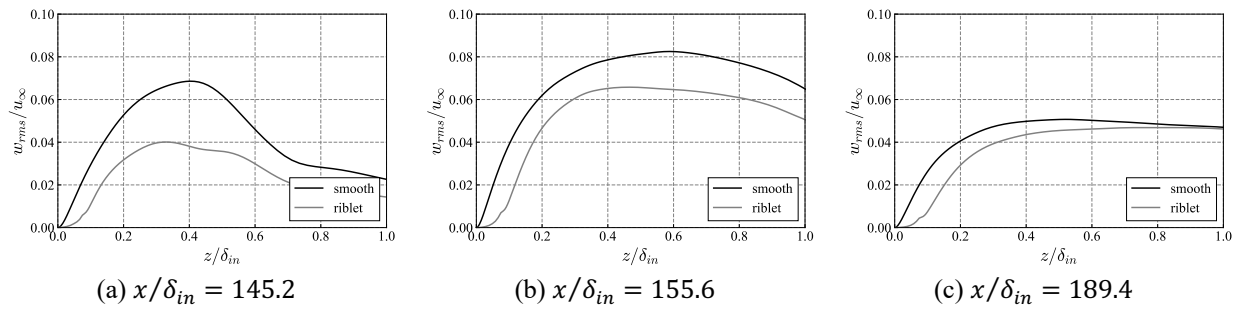


Figure 8 : The time- and spanwise-averaged  $v_{rms}$  profile

From Figure 7 it can be observed that the riblet induces turbulent intensity in the spanwise direction in the vicinity of the inlet, while the riblet suppresses turbulent intensity in the spanwise direction downstream. This trend can also be confirmed from Figure 8. In turbulent flow, the riblet suppresses the turbulence intensity in the spanwise direction, same as in the previous study by Choi et al. [18, 20]. On the other hand, it is newly found that the riblet promotes the collapse of the T-S spanwise vortices.

Next, the visualisations of the  $w_{rms}$  are shown in Figure 9. Figure 9 shows a side view of the region  $x/\delta_{in} = 140\sim 196.6$ , with the flow direction to the right of the paper. The vertical distribution of  $w_{rms}$  at  $x/\delta_{in} = 145.2, 155.6$  and  $189.4$  are also shown in Figure 10.

Figure 9 : Side view contour maps of the time- and spanwise-averaged  $w_{rms}$ Figure10 : The time- and spanwise-averaged  $w_{rms}$  profile

Figures 9 and 10 show that the riblet tends to reduce the turbulent intensity in the wall-normal direction throughout the computational domain. These results suggest that the riblet has the effect of reducing the turbulence intensity in the wall-normal direction for both spanwise and longitudinal vortices.

Finally, the visualisations of the Turbulence Kinetic Energy (TKE) are shown in Figure 11. Figure 11 shows a side view of the region  $x/\delta_{in} = 140 \sim 196.6$ , with the flow direction to the right of the paper.

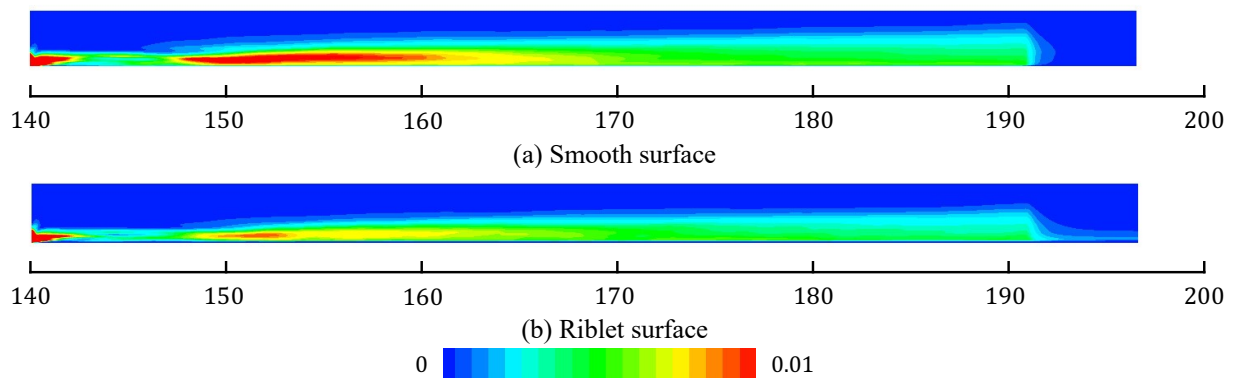


Figure 11 : Side view contour maps of the time- and spanwise-averaged TKE

Figure 11 shows that TKE tends to be suppressed on the riblet surface compared to the smooth surface. This result indicates that the riblet has the same effect as the sand-grind rough surface investigated by Hamada et al. [6]. The location of the peak in TKE is slightly shifted downstream on the riblet surface. The investigation of the turbulence intensity indicate that the riblet suppresses the turbulence intensity in the streamwise and wall-normal direction in the growth process of the T-S waves while enhancing the turbulence intensity in the spanwise direction. In otherwise, the riblet seems to promote three-dimensional collapse before the T-S waves grow strongly. Therefore, the TKE has decreased after the turbulent transition on the riblet surface.

### 3.3 Drag change ratio

The drag change ratio is described in this section. In this analysis, the laminar, transition, and turbulent flow regions are included, and each region is defined based on the computational result on the smooth surface as shown in Figure 12: the location where  $C_F$  becomes the smallest is defined as the switching point from the laminar to the transition region, and the switching point between the transition and the turbulent region is defined as the point where  $C_F$  reaches its peak. In Figure 12, the solid line shows the results of the analysis conducted in this study on the smooth surface and the dashed line is the theoretical solution of  $C_F$  in the turbulent region. Based on this definition, change ratios of drag  $CR_D$  are calculated (i) for only the laminar region, (ii) for only the transition region, (iii) for only the turbulent region, and (iv) for the whole region.

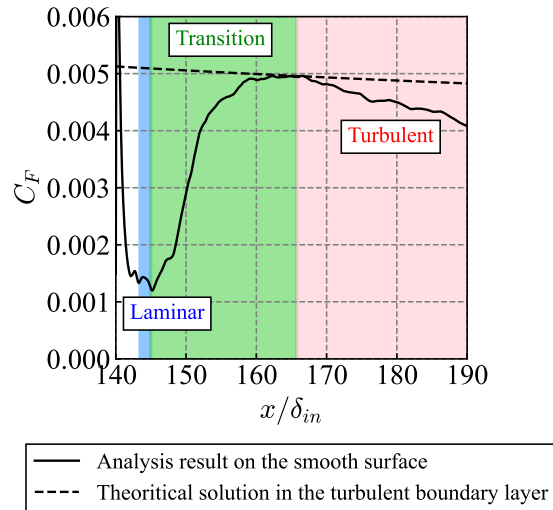


Figure 12 : The definition of the laminar, transition and turbulent region from the time- and spanwise-averaged distribution of the friction drag coefficient on the smooth surface

Table 3 shows the change rate of drag. The values in Table 3 include error ranges determined by standard deviations.

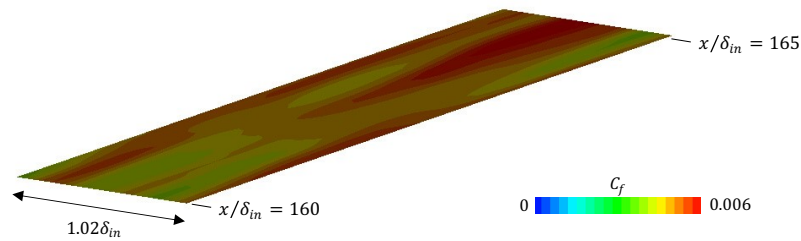
(i) Laminar %	(ii) Transition %	(iii) Turbulent %	(iv) Whole %
$42.9 \pm 79.6$	$-18.8 \pm 2.47$	$-9.03 \pm 2.69$	$-6.24 \pm 2.30$

As shown in Table 3, the drag on the riblet surface in the (iii) turbulent region is reduced by approximately 9.03%. This is almost the same as the results of previous studies for incompressible channel turbulence [14-16], indicating the validity of this analysis. The drag is also reduced in the (ii) transition region by the riblet. On the other hand, the drag in the (i) laminar region is increased. Overall, the riblet reduces the drag in the (iv) whole region.

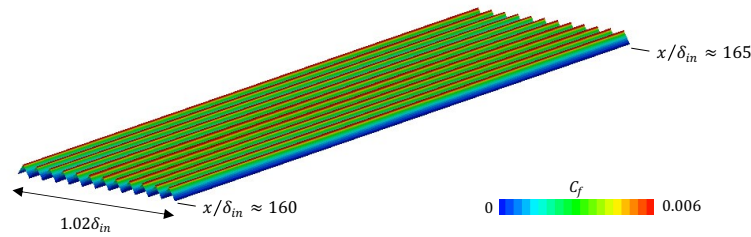
The results described in sections 3.1 and 3.2 suggested that the transition location has changed slightly, but not dramatically, therefore other reasons are considered to be largely contributing to the change in drag. The following sections discuss what is contributing to the change in drag.

### 3.4 Fiction drag coefficient

The influence of the riblet on the friction drag coefficient is investigated. Figure 13 shows the distribution of the friction drag coefficient at  $x/\delta_{in} \approx 160 \sim 165$ . The distribution of the friction drag coefficients on the smooth and riblet surfaces is obviously different, as shown in Figure 13. On the riblet surface, the coefficient of friction drag is large only at the tip, while the value is small in the trough of the ribs.



(a) Smooth surface



(b) Riblet surface

Figure 13 : The distribution of the time-averaged local coefficient of the friction drag

The distributions of the spanwise and spanwise phase average friction coefficient are shown in Figure 14. In Figure 14, the black line, the red line, the green line and the blue line correspond to the results of the smooth, tip of the rib, middle of the rib and valley of the rib, respectively, and the grey solid line corresponds to the spanwise average of the riblet and the grey dashed line corresponds to taking into account the increase in wetting area. On the riblet surface, the tip, middle and valley are the positions marked by the red, green and blue dots in the Figure 15, respectively.

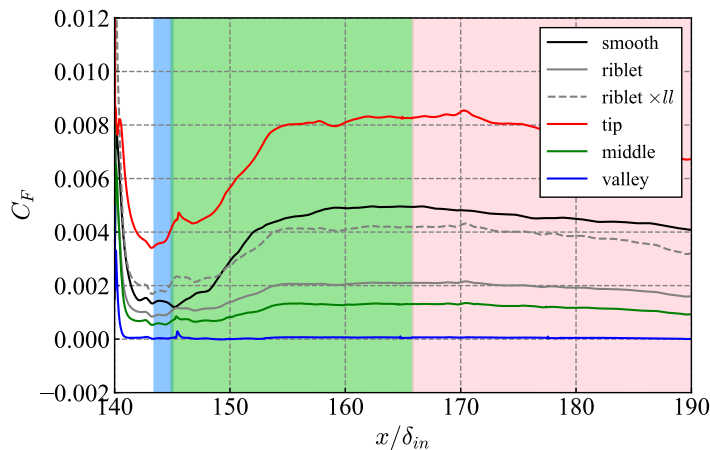


Figure 14 : The distribution of the friction drag coefficient along the streamwise direction

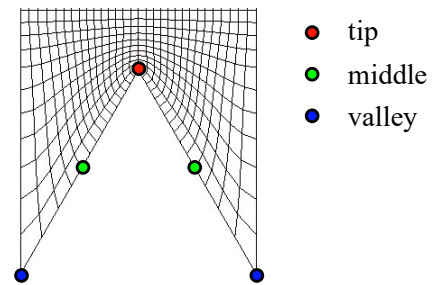


Figure 15 : The locations of tip, middle and valley of the riblet

Figure 14 demonstrates that the friction drag coefficient is higher than the smooth surface at the tip of the ribs; however, it is lower than the smooth surface in the trough, resulting in the average friction coefficient being lower than the smooth surface. Taking into account the increased wetted area of the riblet, the friction coefficient is higher on the riblet surface than on the smooth surface in the laminar region and in some parts of the transition region, whereas the friction coefficient is lower on the riblet surface than on the smooth surface in most of the transition region and in the turbulent region. For this reason, drag increased in the laminar region and decreased the drag in the transition and turbulent regions. The following sections discuss the reasons for the change in the friction drag coefficient on the riblet surface.

The shear stresses in turbulent flow are broadly divided into stresses due to kinematic viscosity and stresses due to turbulence fluctuations. Therefore, the focus is on how each of these stresses is altered by the riblet.

### 3.5 Effects of the riblet on the stresses due to kinematic viscosity

The stress due to kinematic viscosity is directly related to the velocity-gradient near the wall of the mean flow velocity. Accordingly, the time- and spanwise-averaged velocity profiles near the wall at  $x/\delta_{in} = 142.6, 145.2, 155.6$  and  $189.4$  are shown in Figure 16.  $x/\delta_{in} = 142.6$  corresponds to a laminar flow regime,  $x/\delta_{in} = 145.2$  is the transition beginning location,  $x/\delta_{in} = 155.6$  is the transition region and  $x/\delta_{in} = 189.4$  is the turbulent region.

Figure 16 shows that the mean velocity-gradient near the wall is milder on the riblet surface than on the smooth surface in all regions. This result means that the riblet has the effect of reducing the stresses due to kinematic viscosity.

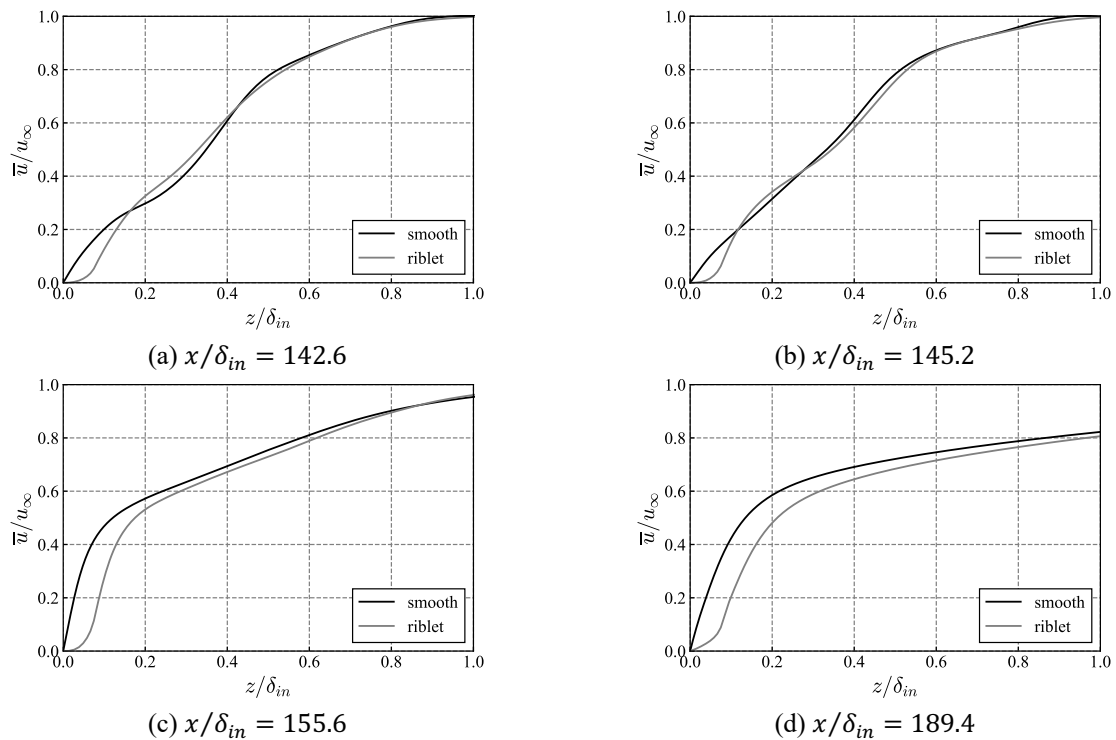


Figure 16 : The time- and spanwise-averaged mean velocity profile

### 3.6 Effects of the riblet on the stresses due to turbulence fluctuations

The Reynolds shear stress is generated in the transition and turbulent regions and contributes to the frictional drag. Therefore, the distributions of the Reynolds shear stress in the transition and turbulent regions at  $x/\delta_{in} = 145.2, 155.6$  and  $189.4$  are shown in Figure 17.

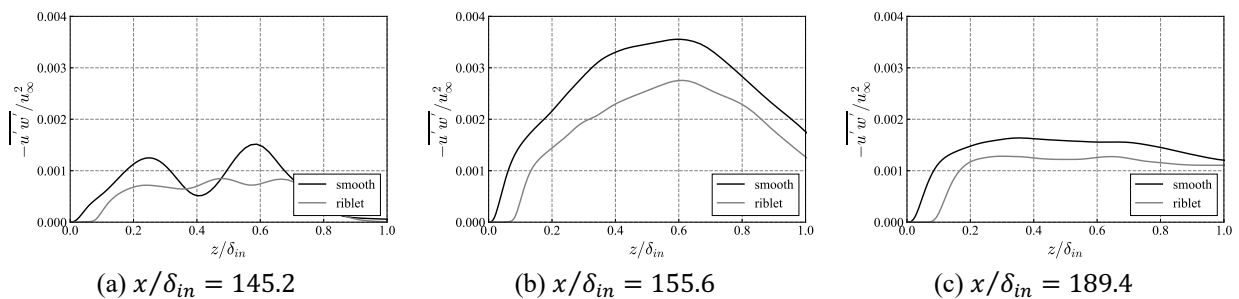


Figure 17 : The time- and spanwise-averaged Reynolds shear stress  $-\overline{u'w'}$  profile

Figure 17 shows that the riblet tends to reduce the Reynolds shear stress compared to the smooth surface. In particular, on the riblet surface, the Reynolds shear stress is suppressed near the wall.

Fukagata et al. [36] proposed the FIK identity, which describes the identity between the friction drag coefficient and the Reynolds shear stress in incompressible turbulent channel, pipe and plane layer flows. Moreover Gomez et al. [37]

extended the FIK identity to compressible flows. Equation (10) is the turbulence contribution term of the FIK identity for the compressible boundary layer on the plane.

$$C_T = 4 \int_0^\delta \rho \left(1 - \frac{z}{\delta}\right) (-\overline{u'w'}) dz \quad (10)$$

Equation (10) is a weighted integral of the Reynolds shear stress. This weighted integral denotes that the closer to the wall surface, the greater the contribution to turbulent friction. The streamwise distribution of the weighted integral of the Reynolds stress,  $C_T$ , is shown in Figure 18.

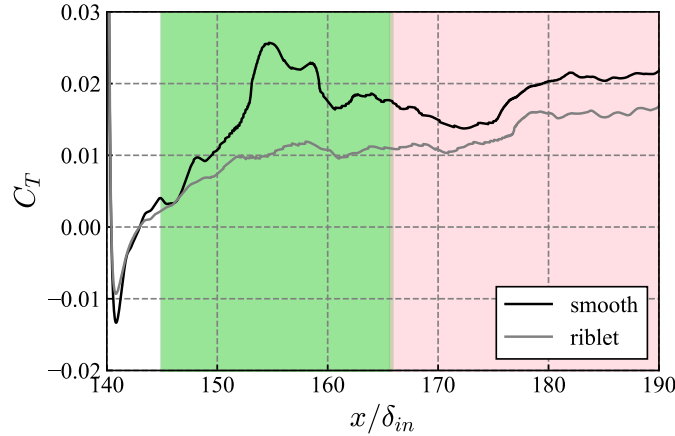


Figure 18 : The time- and spanwise-averaged distribution of the weighte Reynolds shear stress

Figure 18 shows that  $C_T$  is lower on the riblet surface than on the smooth surface in the transition and turbulent regions. This indicates that in addition to the reduction in stress due to kinematic viscosity described in section 3.5, the stress due to turbulent fluctuations is reduced in the transition and turbulent regions, thereby reducing drag. In the laminar region, the only effect of the riblet is a decrease in kinematic viscosity, which is not sufficient to overcome the increase in wetted area, thus the drag is increased. In most of the transition region, it is observed that the decrease in  $C_T$  of the riblet surface relative to the smooth surface is greater than in the turbulent region. This could be due to the fact that the rate of drag reduction is greater in the transition region than in the turbulent region. As discussed in section 3.3, the riblet appears to promote three-dimensional collapse before the T-S waves grow strongly. The decrease in the TKE in the transition region due to this effect and the decrease in  $C_T$  over the riblet surface in the transition region would seem to be related. More detailed investigations of this discussion are required in the future.

#### 4. Conclusion

In this study, DNSs were performed to mainly reveal the effect of the riblet on the drag in the laminar, the transition and the turbulent regions at the speed of the aircraft cruise condition.

From the visualization of the instantaneous iso-surfaces of the second invariant of the velocity gradient tensor, it was found that the location of the beginning of the TS wave collapse does not change significantly between the smooth and riblet surfaces.

Nevertheless, the drag decreased in the transition and turbulent regions while it increased in the laminar region on the riblet surface compared to the smooth surface. The main reason for the change in the drag is that the riblet modified the distribution of the friction drag coefficient. Specifically, the friction drag coefficient became higher than the smooth surface only at the tip of the ribs, whereas it became lower than the smooth surface in the trough. Therefore, the average friction coefficient got lower than the smooth surface. Taking into account the increased wetted area on the riblet surface, the friction drag on the riblet surface increased compared to the smooth surface in the laminar region and in some parts of the transition region, while the friction drag on the riblet surface decreased in most of the transition region and in the turbulent region.

In order to understand the mechanisms of the change in the friction drag coefficient, the effect of the riblet on the stresses due to the kinematic viscosity and the stresses due to the turbulent fluctuations was investigated. As a result, it was found that the kinematic viscosity stresses are reduced on the riblet surface compared to the smooth surface, in both laminar, transition and turbulent flow regions. In the laminar flow regime, only the reduction of the kinematic viscous stresses was apparent as an effect of the riblet; however, this effect is not sufficient to reduce drag enough to exceed the increase in wetted area. On the other hand, in addition to the reduction of the kinematic viscous stresses,

the stresses due to turbulent fluctuations, i.e. Reynolds shear stresses, were suppressed by the riblet in the transition and turbulent regions. As a result, drag decreased in the transition and turbulent regions.

The rate of drag reduction was higher in the transition region than in the turbulent region, one of the reasons being that the reduction in weighted Reynolds stress was greater in the transition region. The investigation of the turbulence statistics suggests that it is due to the suppression of the TKE in the transition region on the riblet surface, as the riblet promotes three-dimensional collapse before the T-S waves grow strongly. It is conceivable that a correlation exists between the reduction in the TKE and the reduction in turbulent friction, although further comprehensive investigations are warranted to confirm the relationship.

## Acknowledgements

The Japan Aerospace Exploration Agency (JAXA) supercomputer system "JSS3" was used for the analysis in this study. This work was supported by JST SPRING, Grant Number JPMJSP2108.

## References

- [1] Reneaux, J. 2004. Overview on drag reduction technologies for civil transport aircraft. In: *European Congress on Computational Methods in Applied Sciences and Engineering*.
- [2] Szodruch, J. 1991. Viscous Drag Reduction on Transport Aircraft. In: *29th Aerospace Sciences Meeting*.
- [3] Michimasa Fujino. 2005. Design and Development of the HondaJet. *Journal of Aircraft*. 43(3).
- [4] Tani, I. 1988. Drag reduction by riblet viewed as roughness problem, *Proceedings of the Japan Academy*. Series B. 6:21–24.
- [5] Oguri, E. and Kohama, Y. 1996. Drag reduction by micro-sized distributed surface geometry on a flat plate. *Transactions of the JSME*. 62:1754–1761.
- [6] S. Hamada, A. Yakeno, S. Obayashi. 2022. Ultra-fine roughness effect on transition delay using direct numerical simulation. In: *12th International Symposium on Turbulence and Shear Flow Phenomena (TSFP)*.
- [7] Wilkinson, S., Anders, J., Lazos, B., and Bushnell, D. 1988. Turbulent Drag Reduction Research at NASA Langley: Progress and Plans. *International Journal of Heat and Fluid Flow*. 9(3):266–277.
- [8] Walsh, M. 1990. Viscous Drag Reduction in Boundary Layers. *Progress in Astronautics and Aeronautics*. 123:203–261.
- [9] Bechert, D., and Bartenwerfer, M. 1989. The Viscous Flow on Surfaces with Longitudinal Ribs. *Journal of Fluid Mechanics*. 206:105–129.
- [10] D. W. Bechert, M. Bruse, W. Hage, J. G. T. Van Der Hoeven and G. Hoppe. 1997. Experiments on drag-reducing surfaces and their optimization with an adjustable geometry. *J. Fluid Mech.* 338:59-87
- [11] Iijima, H., Takahashi, H., Koga, S., Sasamori, M., Iijima, Y., Abe, H., Nishizawa, A., and Kurita, M. 2019. Skin Friction Drag Reduction in Turbulent Boundary Layer Conditions over Riblet Surfaces. In: *AIAA Scitech 2019 Forum*. 1621.
- [12] Kurita, M., Iijima, H., Koga, S., Nishizawa, A., Kwak, D., Iijima, Y., Takahashi, H., and Abe, H. 2020. Flight test for paint-riblet. In: *AIAA Scitech 2020 Forum*. 0560.
- [13] Henry C. Bilinsky, Mitchell S. Quinn, Dylan McGrath, John Whitelock, Swapnil Poudyal, Duncan C. Bell, Christoph Feichtinger, Peter A. Leidl and Richard Benauer. 2023. Materials and Performance Testing of DCM Drag-Reducing Riblets for Aviation. In: *AIAA SCITECH 2023 Forum*.
- [14] M. J. Walsh. 1990. Passive turbulent drag reduction; Riblets. *Prog. in Astro. and Aero.* 123:203-262.
- [15] Douglas C. Chu and George Em Karniadakis. 1993. A direct numerical simulation of laminar and turbulent flow over riblet-mounted surfaces. *J. Fluid Mech.* 250:1-42.
- [16] Walsh, M.J. 1982. Turbulent boundary layer drag reduction using riblets. *AIAA paper*. 82-0169.
- [17] Walsh, M. J. and Lindemann, A. M. 1984. Optimization and application of riblets for turbulent drag reduction. In: *AIAA 2<sup>nd</sup> Aerospace Science Meeting*. 84-0347.
- [18] Haecheon Choi, Parviz Moin and John Kim. 1993. Direct numerical simulation of turbulent flow over riblets. *J. Fluid Mech.* 255:503-539.
- [19] S. –J. Lee and S. –H. Lee. 2001. Flow field analysis of a turbulent boundary layer over a riblet surface. *Experiments in Fluid*. 30:153-166.
- [20] Suzuki, Yuji, and Nobuhide Kasagi. 1994. Turbulent drag reduction mechanism above a riblet surface. *AIAA journal*. 32(9):1781-1790.
- [21] Walsh, M. J., Sellers III, W. L., and Mcginley, C. B. 1989. Riblet drag at flight conditions. *Journal of Aircraft*, 26(6):570-575.
- [22] L. Djenidi et al. 1989. Numerical and experimental investigation of the laminar boundary layer over riblets. *Applied Scientific Research*. 46:263-270.
- [23] L. Djenidi et al. 1994. Laminar boundary layer over riblets. *Physics of Fluids*. 6.

- [24] Haecheon Choi et al. 1991. On the effect of riblets in fully developed laminar channel flows. *Phys. Fluids A*. 3(8).
- [25] Shabnam Raayai-Ardakani et al. 2017. Drag reduction using wrinkled surfaces in high Reynolds number laminar boundary layer flows. *Physics of Fluids*. 29.
- [26] Kaneko, K., Oyama, A., Yakeno, A. 2023. Riblet surface effect study on laminar boundary layer by implicit LES. In: *The Japan Society for Aeronautical and Space Sciences Meeting*. write in Japanese.
- [27] Ladd, D., Rohr, J., Reidy, L., and Hendricks. 1993. The Effect of Riblets on Laminar to Turbulent Transition. *Experiments in Fluids*. 14(1):1-9.
- [28] G. R. Grek, V. V. Kozlov and S. V. Titarenko. 1996. An experimental study of the influence of riblets on transition.. *J. Fluid Mech.* 315:31-49.
- [29] S. Klumpp, M. Meinke and W. Schröder. 2010. LES of Riblet Controlled Temporal Transition of Channel Flow. *Progress in Turbulence III*. 183–186.
- [30] Kozo Fujii. 1990. Developing an accurate and efficient method for compressible flow simulations -example of cfd in aeronautics. *The Proceedings: Fifth International Conference on Numerical Ship Hydrodynamics*.
- [31] Sanjiva K. Lele. 1992. Compact finite difference schemes with spectral-like resolution. *Journal of Computational Physic*. 103(1):16-42.
- [32] Gaitonde, D. V. and Visbal, R. M. 2000. Pade Type High-Order Boundary Filters for the Navier-Stokes Equations. *AIAA Journal*. 38(11):2103-2112.
- [33] Chi-Wang, S. and Osher, S. 1988. Efficient implementation of essentially non-oscillatory shock-capturing schemes. *Journal of Computational Physics*. 77(2):439–471.
- [34] Jie Yao, Xi Chen and Fazle Hussain. 2022. Direct numerical simulation of turbulent open channel flows at moderately high Reynolds numbers. *J. Fluid Mech.* 953.
- [35] A. Busse and T.O. Jelly. 2019. Influence of surface anisotropy on turbulent flow over irregular roughness. *Flow, Turbulence and Combustion*, 104:331–354.
- [36] Fukagata, K., Iwamoto, K., and Kasagi, N. 2002. Contribution of Reynolds stress distribution to the skin friction in wall-bounded flows. *Physics of Fluids*, 14(11):73-76.
- [37] Gomez, T., V. Flutet, and P. Sagaut. 2009. Contribution of Reynolds stress distribution to the skin friction in compressible turbulent channel flows. *Physical Review E*. 79(3):035301.